

# Intravoxel incoherent motion: application in differentiation of hepatocellular carcinoma and focal nodular hyperplasia

Ma Luo\*  
Ling Zhang\*  
Xin-Hua Jiang  
Wei-Dong Zhang

## PURPOSE

We aimed to explore whether intravoxel incoherent motion (IVIM)-related parameters of hepatocellular carcinoma (HCC) and focal nodular hyperplasia (FNH) demonstrate differences that could be used to differentiate and improve diagnostic efficiency.

## METHODS

A total of 27 patients, including 22 with HCC and 5 with FNH, underwent liver 3.0 T magnetic resonance imaging for routine sequences. They were concurrently examined by IVIM diffusion-weighted imaging (DWI) scanning with 11 different b values (0–800 s/mm<sup>2</sup>). IVIM-derived parameters, such as pure diffusion coefficient (D), pseudo-diffusion coefficient (D\*), perfusion fraction (f), and apparent diffusion coefficient (ADC<sub>total</sub>), were quantified automatically by post-processing software and compared between HCC and FNH groups. A receiver operating characteristic (ROC) curve was then created to predict their diagnostic value.

## RESULTS

D\* was weak in terms of reproducibility among the other parameters. ADC<sub>total</sub>, D, and D\* were significantly lower in the HCC group than in the FNH group, while f did not show a significant difference. ADC<sub>total</sub> and D had the largest area under the curve values (AUC; 0.915 and 0.897, respectively) and similarly high efficacy to differentiate the two conditions.

## CONCLUSION

IVIM provides a new modality to differentiate the HCC and FNH. ADC<sub>total</sub> and D demonstrated outstanding and comparable diagnosing utility.

**A**mong primary malignant hepatic tumors, hepatocellular carcinoma (HCC) is the most common disease and is highly associated with chronic hepatitis B and cirrhosis. Focal nodular hyperplasia (FNH) is the second most common benign focal liver lesion (1), and although it displays gentle biological behavior generally, it can cause abdominal pain or right upper quadrant discomfort occasionally. In terms of the extent of vascular supply during contrast enhancement, HCC and FNH both show a hyperarterialization pattern. HCC is characterized by rapid washout in portal and delayed phase compared with adjacent liver tissue, while FNH displays isointensity or mild hyperintensity in the venous phase because of its slower washout. Liver-specific contrast agents, such as gadoxetic acid, can provide unique information to diagnose these conditions more precisely; however, such agents increase the cost and time-consumption of diagnosis. Occasionally, HCC and FNH show confounding or atypical appearances on imaging, especially for high- or middle-grade differentiated HCC, leading to confusion, misdiagnosis (Fig. 1), and even unnecessary interventions. Since the treatment of these two lesions is completely different, avoiding unnecessary invasive treatment or tests, such as biopsy, surgery, or interventional therapy, is vital for the prognosis and quality of life of the patient. Therefore, it is crucial to diagnose these conditions noninvasively and accurately before surgery.

Diffusion-weighted imaging (DWI) is a functional technology to detect diffusion of water molecules and permits to capture more detailed disease information. For lesion detection, the signal intensity on diffusion-weighted image depends on several factors, particularly cell density. Malignant tumors are characterized by heterogeneous cell proliferation, hy-

\*These authors contributed equally to this work.

From the Department of Radiology (W-D.Z. ✉ zhangwd@sysucc.org.cn), Sun Yat-sen University Cancer Center, State Key Laboratory of Oncology in South China, Collaborative Innovation Center for Cancer Medicine, Guangzhou, Guangdong, China.

Received 16 December 2016; revision requested 17 January 2017; last revision received 15 March 2017; accepted 19 March 2017.

DOI 10.5152/dir.2017.16595

You may cite this article as: Luo M, Zhang L, Jiang XH, Zhang WD. Intravoxel incoherent motion: application in differentiation of hepatocellular carcinoma and focal nodular hyperplasia. *Diagn Interv Radiol* 2017; 23:263–271.

percellularity, and decreased extracellular space, making them manifest as hyperintense signal on DWI. The apparent diffusion coefficient (ADC), calculated from two b values, is a quantitative analysis of diffusion that has received significant attention in clinical practice (2, 3). However, the ADC calculated from a mono-exponential fit has been shown to be larger than the true diffusion in voxels, which means traditional DWI and ADC might have been overestimated for lesion analysis in daily practice.

Le Bihan et al. (4) proposed the intravoxel incoherent motion (IVIM) model after proving that perfusion exists inherently in diffusion-weighted image voxels and influences the measurement of the ADC subtly. Both diffusion and perfusion can be quantified or estimated separately by multi-b values according to a bi-exponential model, including  $D$ ,  $f$ , and  $D^*$ , which represent the pure diffusion coefficient, perfusion fraction, and pseudodiffusion coefficient, respectively. Recently, IVIM has become popular and has been applied routinely in the human body, mostly to evaluate therapeutic response (5, 6), in chronic disease assessment (7, 8), and for lesion detection and characterization (9, 10). One of the most conspicuous advantages of IVIM is that it does not require contrast medium injection. It is believed that the IVIM parameters between malignant and benign tumors of the liver are apparently different (11–14); however, these previous reports were of limited use because they included non-solid tumors, such as cysts, abscesses, or hemangiomas; hypovascular metastatic lesions; and ill-defined tumors like cholangiocarcinoma, which are hard to delineate in the analysis.

The aim of the present study was to determine whether IVIM-derived parameters are distinct between HCC and FNH and

whether they can be used to differentiate these solid hyperenhancing tumors noninvasively.

## Methods

### Study selection

This study protocol was approved by the local ethics committee. Informed consent was obtained from all patients before the examination. Inclusion criterion was a suspected FNH or HCC without previous treatment. Between January 2016 and July 2016, we examined 41 patients with clinically suspected FNH ( $n=5$ ) and HCC ( $n=36$ ), as observed by computed tomography (CT) or magnetic resonance imaging (MRI). The exclusion criteria were as follows: (a) no liver nodule or tumor on CT or MRI; (b) lesion diameter  $<1$  cm; and (c) accompanying portal vein tumor thrombus (PVTT) in HCC.

The final study population comprised 5 patients with FNH and 22 patients with HCC (excluding 14 patients with PVTT: 9 PVTTs in the right branch or its sub-branch, 1 in the left branch, and 4 in the trunk or its

bifurcation). In HCC group, there were 21 patients with mild or severe cirrhosis and 1 without obvious cirrhosis. Also, in this group, 16 patients were Hepatitis B surface antigen (HBsAg) positive, 1 patient was HBsAg negative, while 5 patients were not tested in our hospital. The mean age was  $42.0 \pm 9.2$  years (range, 33–52 years) in the FNH group and  $52.6 \pm 13.7$  years (range, 25–79 years) in the HCC group. Histopathologic confirmation was available in 11 patients with HCC (8 patients confirmed after surgery and 3 patients confirmed by biopsy) and in 2 patients with FNH (after surgery). In the remaining patients (11 patients with HCC, 3 with FNH), the lesion was diagnosed using typical imaging features, as well as elevated alpha fetal protein (AFP) in HCCs. According to the guideline of the American Association for the Study of Liver Diseases (AASLD), a nodule larger than 1 cm or a mass can be diagnosed noninvasively using a single dynamic imaging technique that shows intense arterial uptake followed by a washout of contrast in the venous-delayed phase. FNHs are diagnosed by intense arterial uptake and per-

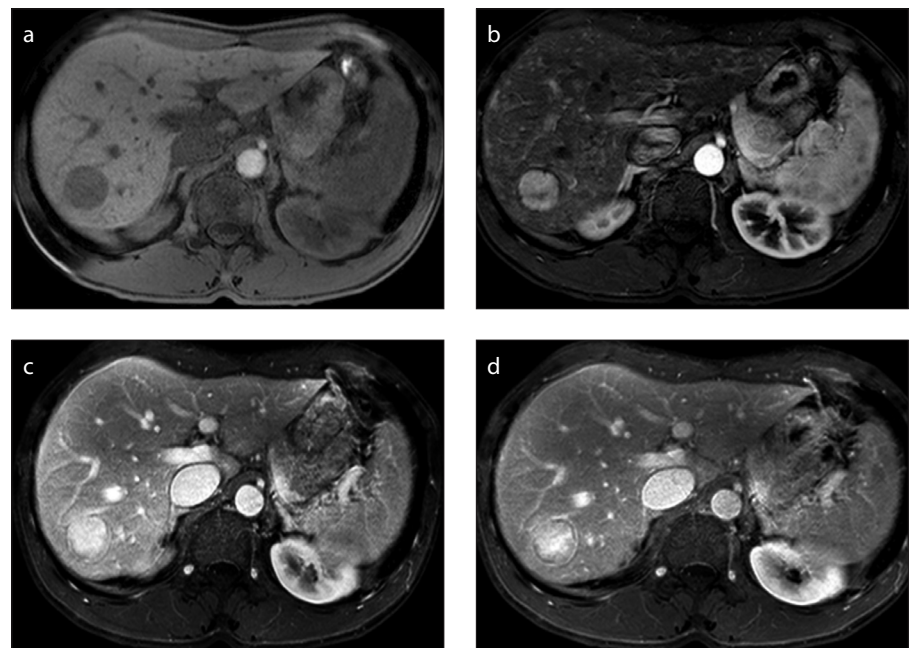


**Figure 1.** a–d. A 45-year-old male with unknown hepatitis B virus infection and alpha fetal protein (-). Axial fat-suppressed T1-weighted unenhanced image (a) shows a hypointense lesion in Segment-VII. An axial fat-suppressed T1-weighted contrast-enhanced image (b) shows a slightly heterogeneous hypervascular lesion with a small focal area of hypointensity. The lesion still demonstrates hyperintensity compared with the surrounding liver parenchyma on portal and equilibrium phase, respectively (c, d). Notably, there is delayed enhancement of the central linear area and peripheral capsule around the lesion. This lesion contains characteristics of both hepatocellular carcinoma (HCC) and focal nodular hyperplasia (FNH), and it is hard to make the correct diagnosis without a hepatocyte-specific contrast agent. The lesion was pathologically proven to be an HCC with intermediate-differentiation after resection.

### Main points

- Intravoxel incoherent motion diffusion-weighted imaging (IVIM-DWI) might be helpful to noninvasively differentiate hepatic solid hypervascular tumors: hepatocellular carcinoma (HCC) and focal nodular hyperplasia (FNH).
- The IVIM-derived parameters, such as pure diffusion coefficient ( $D$ ), pseudo-diffusion coefficient ( $D^*$ ), and  $ADC_{total}$  were significantly different between HCC and FNH.
- $D^*$  was weak for reproducibility among IVIM-derived parameters.

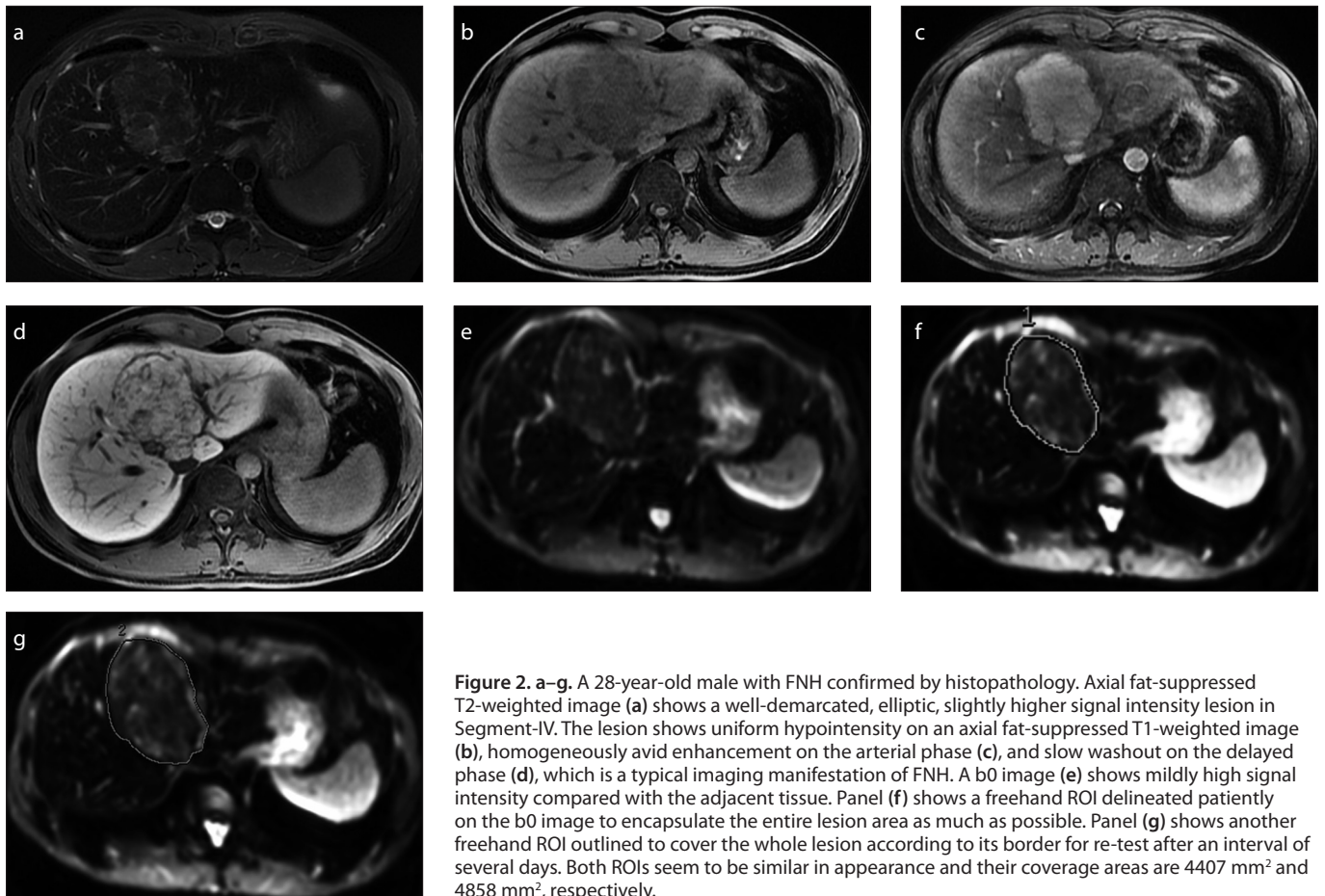


**Figure 2. a–g.** A 28-year-old male with FNH confirmed by histopathology. Axial fat-suppressed T2-weighted image (a) shows a well-demarcated, elliptic, slightly higher signal intensity lesion in Segment-IV. The lesion shows uniform hypointensity on an axial fat-suppressed T1-weighted image (b), homogeneously avid enhancement on the arterial phase (c), and slow washout on the delayed phase (d), which is a typical imaging manifestation of FNH. A b0 image (e) shows mildly high signal intensity compared with the adjacent tissue. Panel (f) shows a freehand ROI delineated patiently on the b0 image to encapsulate the entire lesion area as much as possible. Panel (g) shows another freehand ROI outlined to cover the whole lesion according to its border for re-test after an interval of several days. Both ROIs seem to be similar in appearance and their coverage areas are 4407 mm<sup>2</sup> and 4858 mm<sup>2</sup>, respectively.

sistent enhancement at the late phase or hepatobiliary phase after application of a liver-specific contrast agent.

#### Data acquisition

The patients were examined and evaluated prospectively using a 3.0 T MRI scanner (Discovery 750W, GE Healthcare) with a 16-element body coil. The scan comprised axial fat suppressed respiratory triggered Propeller T2-weighted imaging (TR/TE, 7000–10000/96–100; array, 256×256; slice/gap, 5/1 mm; field of view [FOV], 40 cm), coronal respiratory triggered single shot fast spin-echo T2-weighted imaging (TR/TE, 2000/70 for coronal; slice/gap, 5/1 mm; FOV, 38 cm), breath-hold two-dimensional axial in- and opposed-phase T1-weighted imaging (TR/TE, 5.2/2.2–1.1; slice/gap, 1/1 mm), and axial three-dimensional GRE T1-weighted imaging (LAVA TR/TE, 5.25/1.69; slice thickness, 1/1 mm; FOV, 38 cm) before and after contrast injection (0.01 mmol/kg of gadopentetate dimeglumine [Magnevist, n = 21] and 10 mL fixed dose of gadoxetic acid [Primovist, n=6]). Contrast-enhanced images were acquired

at the arterial phase, portal venous phase (60 s), and delayed phase (180 s). Hepatobiliary phase images were obtained at 15 and 20 min in patients who were injected with gadoxetic acid.

#### Parameters for DWI

Respiratory-triggered single-shot DWI spin-echo planar imaging with multiple b values was carried out. For patients receiving gadoxetic acid, the DWI was performed before the hepatobiliary phase (about 15 min after contrast injection). For the remaining patients, the images of DWI were obtained before administration of gadopentetate dimeglumine (unenhanced images). The scanning parameters were as follows: TR/TE, 6000–10000/61–63.6 ms; FOV, 40 × 40 cm; thickness/spacing, 5/1 mm; bandwidth, 250 kHz; 15 slices, slice thickness/gap = 5/1 mm; spectral fat saturation; ASSET acceleration factor of two; b values = 0, 10, 20, 30, 50, 80, 100, 200, 400, 600, and 800 s/mm<sup>2</sup>; number of excitations, 4. The orthogonal gradient directions were three. The totally average acquisition time of DWI was 5 minutes and 10 seconds.

#### Image analysis

To obtain ADC<sub>total</sub> and IVIM-related parameters, an abdominal radiologist placed regions of interest (ROIs) on diffusion-weighted images at b values of 0 s/mm<sup>2</sup> for each targeted lesion. If a lesion demonstrated homogeneous imaging (Fig. 2), a freehand ROI was drawn carefully along the lesion edge to encompass as much tissue as possible on the slice showing the largest level, or the upper or lower one section of the tumor, avoiding surrounding vessels or bile ducts seen macroscopically. If a lesion showed a heterogeneous appearance in an image (Fig. 3), 3 identical circular ROIs were set on the largest slice to measure viable tumor areas, while avoiding necrosis or cystic change, or hemorrhage zone and artifacts. The average values within each ROI for all parameters were generated by GE post-processing software automatically.

According to the relationship between signal intensities and b values, IVIM could be expressed by a mathematical formula as follows:

$$S_b/S_0 = (1-f) \exp(-bD) + f \exp(-bD^*) \text{ Eq. (1)}$$

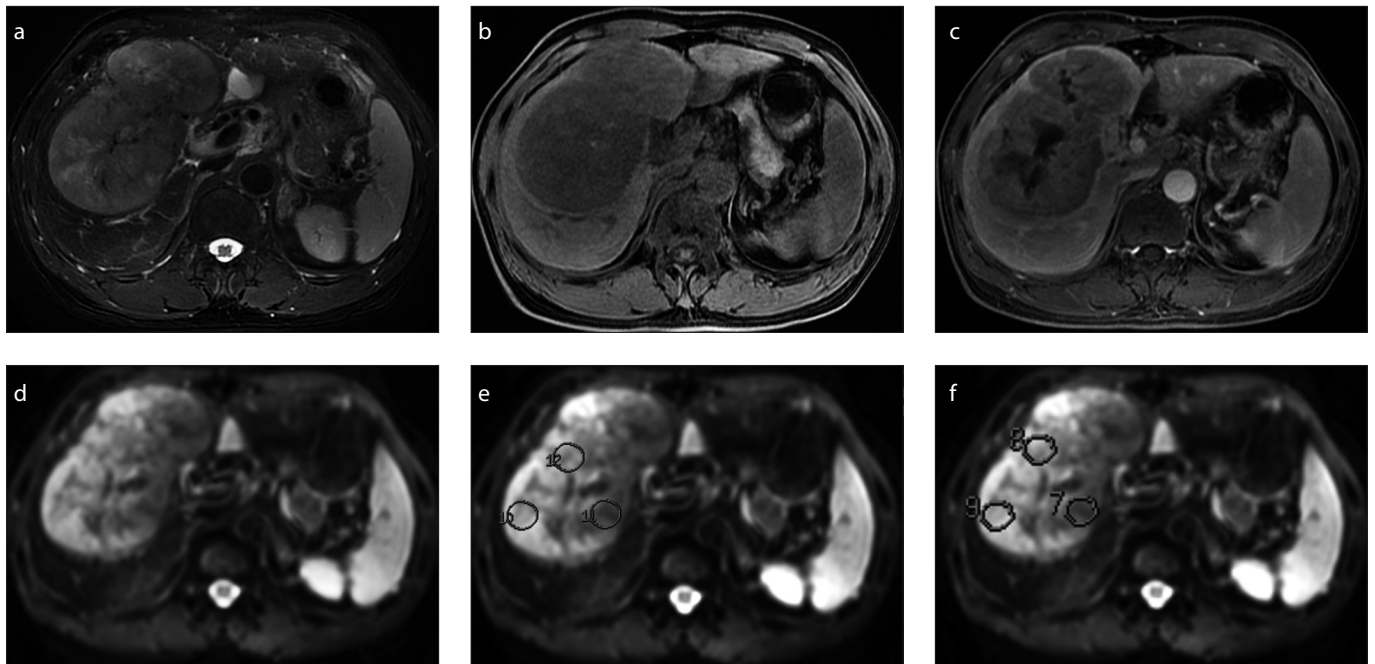


**Figure 3. a–f.** A 59-year-old male with HCC. An axial fat-suppressed T2-weighted image (a) shows a well-circumscribed and lobulated mass that demonstrates a moderately higher signal intensity. An axial fat-suppressed T1-weighted image (b) shows hypointensity and equilibrium phase (c) shows inhomogeneous enhancement. Additionally, the lesion is apparently hypointense compared with the normal liver parenchyma. On b0 image (d), the large mass shows hyperintensity. Three circular ROIs, drawn because of the heterogeneous component, of the same size were set on solid and viable tumor zones on a b0 image (e), according to a regular MRI sequence; care was taken to avoid multiple internal foci of the necrosis area. After a short interval of several days, three identical circular ROIs were placed on the same site for re-test (f).

Where,  $S_0$  = signal intensity at  $b_0$ ;  $S_b$  = signal intensity for a given  $b$  value.

$D^*$  was markedly larger than  $D$ , therefore,  $D$  was calculated by the following equation when the  $b$  value was greater than  $200 \text{ s/mm}^2$  (perfusion content had decayed almost completely at this setting):

$$S_b/S_0 = \exp(-bD) \text{ Eq. (2)}$$

$D^*$  and  $f$  were estimated using the Levenberg–Marquardt method that fitted  $S_b$  for all  $b$  values using Eq. (1) with a fixed  $D$ , and subsequently,  $f$  and  $D^*$  were acquired.

The  $ADC_{total}$  was then calculated by fitting  $b_0$  and all  $b$  values great than or equal to  $200 \text{ s/mm}^2$  for each image ( $200, 400, 600, \text{ and } 800 \text{ s/mm}^2$ ) to a classical linearized mono-exponential model, such that the conventional ADC equation was expressed as:

$$S_b/S_0 = \exp(-bADC) \text{ Eq. (3)}$$

### Statistical analysis

Unless otherwise specified, data are reported as mean  $\pm$  standard deviation. To estimate reproducibility and stability of the repeated measurements, the coefficient of variation (CV) and Bland-Altman (BA) analyses were performed to test data reliability.

The reproducibility of a parameter was defined as excellent when the CV was  $\leq 10\%$ , good when the CV was between  $10\%–20\%$ , acceptable when the CV was between  $20\%–30\%$ , and poor when CV was  $>30\%$ .

Since the same method was used twice for measurement, the mean difference should be zero. Thus, the coefficient of repeatability (CR) could be calculated as  $2 \times$  the standard deviation of the differences between the two measurements ( $d_2$  and  $d_1$ ):

$$CR = 1.96 \times \sqrt{\frac{\sum (d_2 - d_1)^2}{n}}$$

The uniform sizes of circular ROIs were copied for heterogeneous lesions and free-hand ROIs were drawn for homogeneous lesions during re-test analysis. The locations of the ROIs were maintained the same as much as possible to reduce measurement bias.

The nonparametric Mann-Whitney U test was used throughout the study to compare IVIM parameters and  $ADC_{total}$  between HCC and FNH. Parameters that yielded statistical significance between the two groups were assessed by a receiver operating characteristic (ROC) curve to estimate diagnostic performance. All analyses were performed using SPSS version 19.0 (IBM Inc.) and MedCalc Statistical Software. A significant difference was accepted when the  $P$  value was  $<0.05$ .

## Results

We evaluated 22 HCC patients (14 patients had 1 lesion, 2 patients had 2 lesions, 1 patient had 3 lesions, and 5 patients had more than 3 lesions) and 5 FNH patients (5 lesions). The mean lesion diameter was  $77.00 \pm 37.59 \text{ mm}$  and  $42.00 \pm 17.38 \text{ mm}$  for HCCs and FNHs, respectively.

According to the signal intensity acquired from the 11  $b$  values used in our study, the relationship between signal intensity versus  $b$  values could be described as a bi-exponential model for both HCC and FNH.

The stability and reproducibility of all parameters are shown in Table 1. Stability was acceptable for  $ADC_{total}$  and  $D$  (CV of 26.38% and 27.36% for both  $ADC_{total}$  measurements, 27.99% and 28.67% for both  $D$  measurements), and poor for  $f$  and  $D^*$  (CV of 43.41% and 38.65% for both  $f$  measurements, 74.19% and 73.84% for both  $D^*$  measurements), especially for  $D^*$ . The reproducibility results were similar to the stability results, in that  $ADC_{total}$  and  $D$  were better,  $f$  was worse, and  $D^*$  was the worst (a CR of 0.26 for  $ADC_{total}$ , 0.18 for  $D$ , 8.08 for  $f$ , and 53.17 for  $D^*$ ).

The results of the IVIM parameters and  $ADC_{total}$  between HCC and FNH are shown

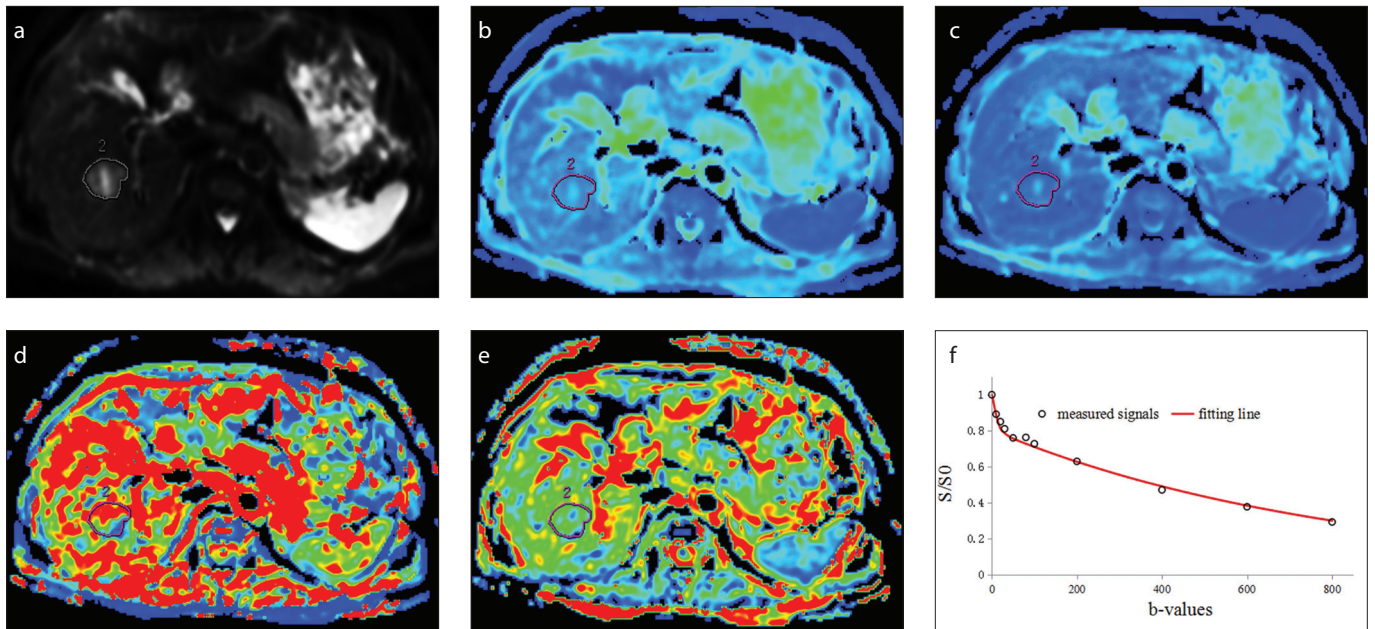


**Figure 4.** a–f. IVIM-DWI with 11 b values (ranging, 0–800 s/mm<sup>2</sup>) from a 53-year-old woman with FNH. Diffusion-weighted image (a) shows a freehand ROI. Parametric images facilitated the presentation of FNH: (b)  $ADC_{total} = 1.61 \times 10^{-3} \text{ mm}^2/\text{s}$ , (c)  $D = 1.23 \times 10^{-3} \text{ mm}^2/\text{s}$ , (d)  $D^* = 93.3 \times 10^{-3} \text{ mm}^2/\text{s}$ , (e)  $f = 19.7\%$ . Panel (f) shows signals decaying bi-exponentially with b value, as shown by the fitting curve (red line). Within the range of low b values (<200 s/mm<sup>2</sup>), the fitting curve demonstrates a large slope, while at large b values (>200 s/mm<sup>2</sup>) the fitting curve demonstrates a gradually declining curve. ADC, apparent diffusion coefficient; D, diffusion coefficient; D\*, pseudo-diffusion coefficient; f, perfusion fraction; IVIM, intravoxel incoherent motion.

**Table 1.** Stability and reproducibility of IVIM-derived parameters and  $ADC_{total}$  in HCC and FNH

	$ADC_{total}$	D	D*	f
CV <sub>1</sub> (%)	26.38	27.99	74.19	43.41
CV <sub>2</sub> (%)	27.36	28.67	73.84	38.65
CR	0.26	0.18	53.17	8.08

IVIM, intravoxel incoherent motion; ADC, apparent diffusion coefficient; HCC, hepatocellular carcinoma; FNH, focal nodular hyperplasia; D, diffusion coefficient; D\*, pseudo-diffusion coefficient; f, perfusion fraction; CV, coefficient of variation; CR, coefficient of repeatability.

**Table 2.** Comparison of IVIM-derived parameters and  $ADC_{total}$  between HCC and FNH

	HCC	FNH	P*
$ADC_{total}$ ( $\times 10^{-3} \text{ mm}^2/\text{s}$ )	1.23±0.23	1.82±0.59	0.001
D ( $\times 10^{-3} \text{ mm}^2/\text{s}$ )	0.95±0.22	1.42±0.35	0.002
D* ( $\times 10^{-3} \text{ mm}^2/\text{s}$ )	75.34±47.72	166.64±114.47	0.026
f (%)	18.29±8.21	22.04±7.32	0.189

IVIM, intravoxel incoherent motion; ADC, apparent diffusion coefficient; HCC, hepatocellular carcinoma; FNH, focal nodular hyperplasia; D, diffusion coefficient; D\*, pseudo-diffusion coefficient; f, perfusion fraction; \*Mann-Whitney U test.

in Table 2.  $ADC_{total}$ , D, and D\* were all significantly lower in the HCC group compared with those in the FNH group ( $P < 0.05$ ).  $ADC_{total}$  values were  $(1.23 \pm 0.23) \times 10^{-3} \text{ mm}^2/\text{s}$  and  $(1.82 \pm 0.59) \times 10^{-3} \text{ mm}^2/\text{s}$  in HCC and FNH, respectively; D values were  $(0.95 \pm 0.22) \times 10^{-3} \text{ mm}^2/\text{s}$  and  $(1.42 \pm 0.35) \times 10^{-3} \text{ mm}^2/\text{s}$ , respectively; and D\* values were  $(75.34 \pm 47.72) \times 10^{-3} \text{ mm}^2/\text{s}$  and  $(166.64 \pm 114.47) \times 10^{-3} \text{ mm}^2/\text{s}$ , respectively.

The f value was not significantly different between HCC and FNH ( $P > 0.05$ ); f values were  $18.29\% \pm 8.21\%$  and  $22.04\% \pm 7.32\%$ , respectively (Figs. 4 and 5).

The ROC analysis demonstrated that  $ADC_{total}$ , D, and D\* could be used to distinguish HCC from FNH, with an excellent diagnostic ability (Fig. 6). The maximum AUC value was seen in  $ADC_{total}$  (AUC=0.915), followed by D (AUC=0.897),

and D\* (AUC=0.805). Highest sensitivity and specificity rates were obtained with cutoffs set to  $1.535 \times 10^{-3} \text{ mm}^2/\text{s}$ ,  $1.055 \times 10^{-3} \text{ mm}^2/\text{s}$ , and  $90.55 \times 10^{-3} \text{ mm}^2/\text{s}$  for  $ADC_{total}$ , D, and D\*, respectively (Table 3).

## Discussion

Unlike the two b values in DWI from which ADC is calculated according to the mono-exponential model, which mixes diffusion as well as blood flow, IVIM can distinguish diffusion and perfusion components separately using multiple b values through a bi-exponential model algorithm (15, 16). This model can be described using the parameters D, D\*, and f, where the latter two parameters represent perfusion-related diffusion.

With respect to ROI placement, accurate measurements are unavoidably influenced by different ROI sizes or locations each time. To eliminate these two factors, we manually placed uniform-sized ROIs at almost the same location as much as possible for each measurement. Our results demonstrated that the CR of D\* was largest among all parameters, which meant that D\* was the least stable. Although we tried to maintain ROI location identical for best endeavors during each operation, it was inevitable that there would still be small differences between

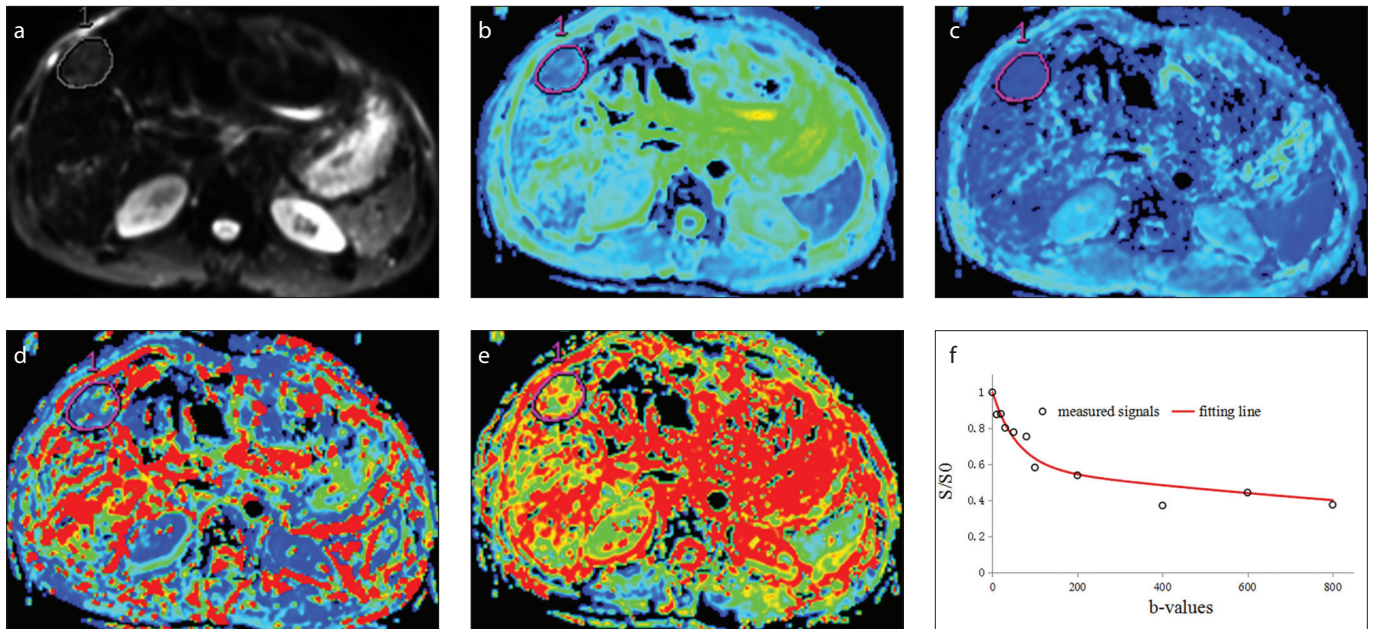


**Figure 5.** a–f. IVIM-DWI with 11 b values (ranging, 0–800 s/mm<sup>2</sup>) from a 57-year-old woman of hepatocellular carcinoma (HCC). Diffusion-weighted image (a) shows a freehand ROI. Parametric images facilitated the presentation of HCC: (b)  $ADC_{total} = 1.52 \times 10^{-3} \text{ mm}^2/\text{s}$ , (c)  $D = 0.467 \times 10^{-3} \text{ mm}^2/\text{s}$ , (d)  $D^* = 29 \times 10^{-3} \text{ mm}^2/\text{s}$ , (e)  $f = 46.7\%$ . Panel (f) shows signals decaying bi-exponentially with b value, as shown by the fitting curve (red line). Within the range of low b values (<200 s/mm<sup>2</sup>), the fitting curve demonstrates a large slope, while at large b values (>200 s/mm<sup>2</sup>) the fitting curve demonstrates a gradually declining curve. ADC, apparent diffusion coefficient; D, diffusion coefficient; D\*, pseudo-diffusion coefficient; f, perfusion fraction; IVIM, intravoxel incoherent motion.

**Table 3.** ROC analysis of  $ADC_{total}$ , D, and D\* for prediction and diagnostic performance between HCC and FNH

HCC vs. FNH	AUC	Cutoff ( $\times 10^{-3} \text{ mm}^2/\text{s}$ )	Sensitivity (%)	Specificity (%)
$ADC_{total}$	0.915	1.535	80.0	94.9
D	0.897	1.055	100	74.4
D*	0.805	90.55	80.0	74.4

ROC, receiver operating characteristics; ADC, apparent diffusion coefficient; D, diffusion coefficient; D\*, pseudo-diffusion coefficient; HCC, hepatocellular carcinoma; FNH, focal nodular hyperplasia; AUC, area under the curve.

two measurement intervals because of the manual operation. Despite this condition,  $ADC_{total}$  and D were the most repeatable, and f showed some good repeatability. Our results confirmed that D\* intrinsically fluctuates, as was shown by other studies (17–19). However, the range of the CR (Bland-Altman) in our study was smaller and reasonably acceptable compared with previous studies (20, 21), which could be explained by our homogeneous ROI placement scheme.

Some patients were subjected to contrast enhancement before regular MRI, such as T1- and T2-weighted imaging and DWI, since liver-specific contrast agents have to be injected first for adequate hepatocyte uptake. A couple of previous studies showed that the effect of contrast medium on imaging parameters was unapparent and did not reach statistical significance (22, 23); therefore, our results were not like-

ly to be influenced by the timing of contrast agent injection.

Increases in cell density or cell swelling and the viscosity of the extra- or intracellular matrix mean that the extracellular space (the distance that water molecules can move unrestricted from one cell to another) decreases. Malignant tumors of the liver, such as HCC, are characterized by hypercellularity and high nucleus-cytoplasm ratios, which are the two major factors that reduce extracellular space, leading to lower diffusion compared with FNH. FNH is composed of normal hepatocytes and malformed bile ducts, in which diffusion is unhampered, as was reflected in our results, where D was lower in HCC than in FNH.

A number of studies have pointed out that perfusion parameters between malignancy and benignity are absolutely different because of their microstructure dispar-

ities (11, 12); however, the nature of these differences in specific lesions is still not completely understood (24–26). Images captured during routine work in hospitals or from the literature for HCC and FNH show that both of these lesions are characterized by abundant blood supply in the arterial phase. Based on the above pathophysiologic feature, some studies have investigated useful ways to distinguish them, because it remains a challenge to make an accurate diagnosis in some complex cases. Klaus et al. (27) found no significant differences between the D\* values of HCCs and FNHs. Nevertheless, an obvious distinction in the D\* values was observed in our study. In addition, the values for D\* and f in our study were larger than those in Klaus et al. (D\*,  $45.7 \pm 54.1$  for HCC and  $39.9 \pm 47.2$  for FNH; f,  $13.6 \pm 6.5$  for HCC and  $14.4 \pm 5.8$  for FNH), and the D\* value for FNH was larger than that for HCC as well. There are three possible explanations for the contradiction between the two datasets. First, the MRI platform is not uniform; we used GE 3.0 T MRI scanner only, while Klaus et al. (27) used two different imagers, although both of them were Siemens 1.5 T (Aera and Magentom Avanto). Barbieri et al. (28) compared different scanners and determined that the IVIM parameters across MRI imagers were substantially different, even between scanners from the

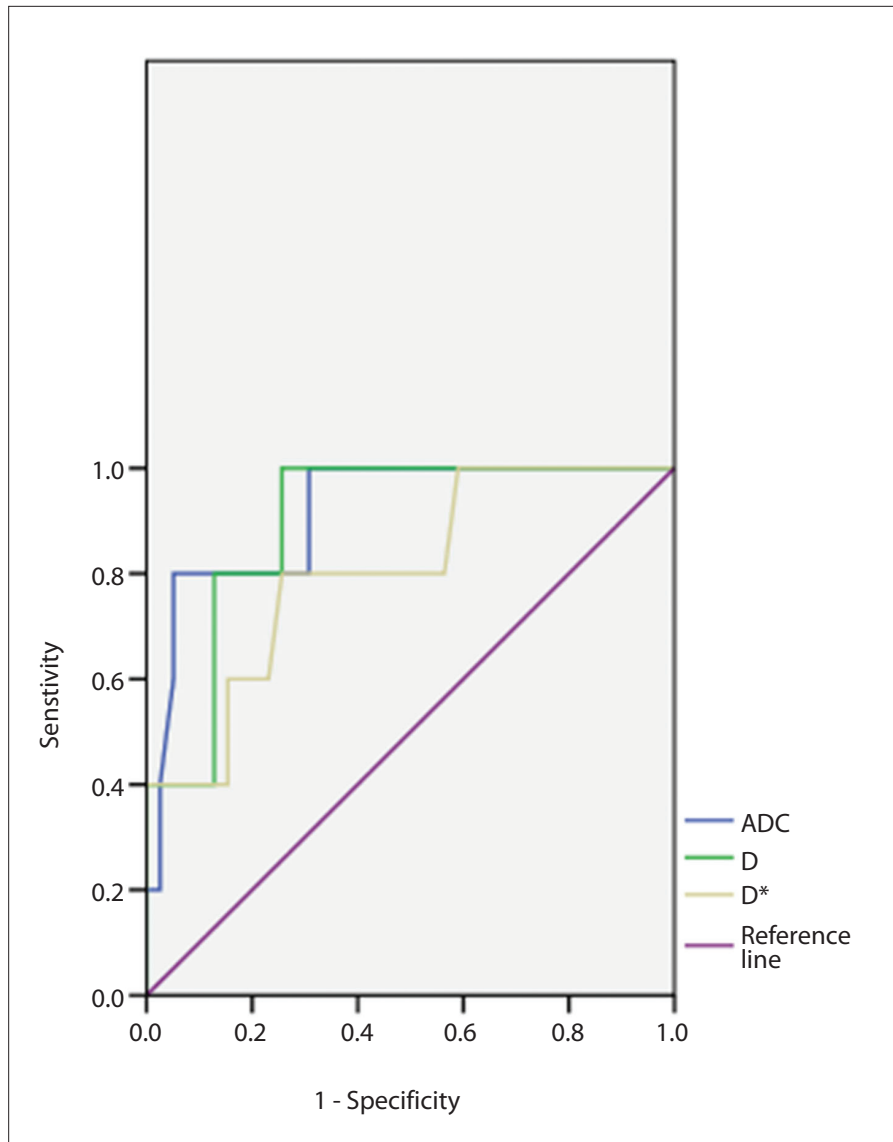


**Figure 6.** ROC curve generated according to  $ADC_{total}$ ,  $D$ , and  $D^*$  values. The cutoff points for  $ADC_{total}$ ,  $D$ , and  $D^*$  were determined as  $1.535 \times 10^{-3} \text{ mm}^2/\text{s}$ ,  $1.055 \times 10^{-3} \text{ mm}^2/\text{s}$ , and  $90.55 \times 10^{-3} \text{ mm}^2/\text{s}$  for hepatic solid hypervascular tumors. At an  $ADC_{total}$  of  $1.535 \times 10^{-3} \text{ mm}^2/\text{s}$ , the sensitivity and specificity for the prediction were 0.800 and 0.949, respectively. At a  $D$  value of  $1.055 \times 10^{-3} \text{ mm}^2/\text{s}$ , the sensitivity and specificity for the prediction were 1 and 0.744, respectively. At a  $D^*$  value of  $90.55 \times 10^{-3} \text{ mm}^2/\text{s}$ , the sensitivity and specificity for the prediction were 0.800 and 0.744, respectively. The ROC curves demonstrated that  $ADC_{total}$  had a slightly higher AUC than  $D$  and  $D^*$ . ROC, receiver operating characteristic; ADC, apparent diffusion coefficient;  $D$ , diffusion coefficient;  $D^*$ , pseudo-diffusion coefficient.

same company but different subtypes, as well as the measurement reproducibility. Moreover, Kakite et al. (20) also showed that different field magnitudes influenced measurement consistency, which resulted from susceptibility artifacts and heterogeneous image quality. Second, including PVTT in the HCC group could be an important determinant of the different results. PVTT sometimes occurs in HCC but not in FNH, so we excluded PVTT in the HCC group, whereas Klaus et al. (27) did not mention PVTT.

Blood flow into the liver supplied by portal vein accounts for approximately 75%–80% in the normal state. The evolution of HCC is characterized by an increase in arterial supplementation; however, a decreased portal flow resulting from PVTT or portal hypertension is not sufficiently compensated for by this increase in arterial flow. Additionally, some patients in our study suffered from severe cirrhosis, mostly caused by hepatitis B, leading to portal vein blood reduction. The remodeling of the hepatic lobule in cir-

rhosis is prone to result in diminished liver perfusion in spite of arterial vasodilatation (29, 30). Furthermore, HCC is notorious for disruption and invasion of hepatic vessels and the parenchyma, in which many tortuous and immature tumor vasculatures and tissues are distributed within a lesion, representing the primary pathologic changes that differ from FNH. These underlying reasons could have caused the discrepancy between the two studies, and we considered that we were more precise in selecting and dividing the study population.

Interestingly, differences in  $f$  values did not reach statistical significance, which seemed paradoxical. Theoretically,  $D^*$  and  $f$  are both perfusion-related parameters and provide perfusion information; therefore, they should have some degree of relationship. However, they reflect different aspects of perfusion:  $D^*$  is related to the length and velocity of the capillary network, whereas  $f$  reflects the fraction of the microcirculation that accounts for all diffusion in voxels. Unsurprisingly, several studies have observed similar mismatches for  $D^*$  and  $f$  (29, 31–33), even in dynamic contrast enhancement research (34), which is another type of perfusion-related hemodynamic model. One convincing explanation for this contradiction is that  $f$  is dependent on echo time (TE): the longer the TE, the larger the  $f$  value. During our scanning, the TE was not constant for each patient because of irregular respiration or variations in liver sizes. Another interpretation is that  $f$  is potentially sensitive to other bulky flow information, such as excretion of granules or glands, diffusion direction or diffusion pattern, and is not specific to perfusion uniquely (35–37). FNH contains bile ducts; therefore, after taking up a hepatocyte-specific contrast agent, delayed biliary excretion is possible. Lastly, the background for state of the organ, such as the liver fat content, fibrotic tissue fraction, and even chronic disease such as pancreatitis, could have considerable influences on the measurement of parameters (7, 38, 39).

ADC itself, containing diffusion and perfusion components, is not able to separate these two components and its practical effectiveness to diagnose or distinguish conditions may be limited to some extent (10, 11, 40). However, previous studies indicated that ADC could be used as a marker to differentiate disease entities because of its high efficacy and ease of calculation

compared with multi-b values (24–27). Our results also showed that  $ADC_{total}$  slightly exceeded D in terms of maximum AUC values, with higher sensitivity and specificity, but there was no statistical difference between them ( $P = 0.61$ ), which meant that  $ADC_{total}$  and D had the same practical effectiveness. On the other hand, we calculated  $ADC_{total}$  from 11 b values instead of  $ADC_{2b}$  from two b values, and did not make comparison between these two indexes.  $ADC_{total}$  has been proven to be superior to  $ADC_{2b}$  (11, 25), because it contains more information. Although Klaus et al. (27) considered that the AUC of D was slightly better than that of ADC, they only used two b values (0 and 800) to calculate their  $ADC_{2b}$ . Further study is warranted to determine whether ADC or D which is more valuable for disease differentiation. Additionally, it should be noted that it is imprecise to fit the bi-exponential model for too few b values, although one report confirmed that only four b values were sufficient to estimate IVIM parameters (41). The SD or CV of  $D^*$  is frequently large and is well known for its worse reproducibility and repeatability compared with the other three parameters (21, 34, 42, 43). In spite of significant differences in the  $D^*$  values between HCC and FNH, its efficacy was inferior to  $ADC_{total}$  and D, as is generally accepted.

The values in our study for  $ADC_{total}$  (2, 27), D (26, 44), and f (24, 45) were in line with or similar to those results reported previously. Our  $D^*$  values were out of range of other studies, especially for FNH (24, 27). Differences in triggering methods, use various b values for scanning, and the sample size are common explanations. Differences in histologic grade might also be a factor; some authors have argued that different tumor grades could affect IVIM parameters (45). Also, feeding could lead to higher parameters, resulting from portal vein dilation, increases in venous blood, and enlarged gastrointestinal tract extrusion adjacent to the liver, compared with fasting. Thus, fasting or not fasting might have potentially contributed to these discrepancies (46).

Several limitations exist in our study. First, the sample number for FNH is small. In contrast to HCC, the incidence of FNH is extremely low, although it is the second most common benign tumor in the liver. There may have been enrollment bias in our study. Ichikawa et al. (12) and Yoon et al. (11) reported one and nine FNH cases, in their study populations, which comprised 84 and 142 patients in total, respectively.

Second, the pathology for some patients was not obtained. Diagnostic criteria for patients without proven histology were based on typical imaging features and relevant laboratory examination. In addition, the histopathologic grades of HCC were not subdivided in our group because this topic was beyond our purpose and we simply focused on the difference between HCC and FNH. However, Woo et al. (45) found that different histologic grades and the enhancement degree of HCC resulted in different parameters. In addition, some ROIs were chosen in the left liver lobe. Lesions located in the left lobe, especially close to the edge of the liver, are susceptible to be affected by cardiac or diaphragm motion and gastrointestinal peristalsis (47–49). It is recommended to select lesions located in the center of the right liver lobe because it is more stable and leads to less overestimation during measurements (50); adding echocardiography triggering could decrease parametric variability effectively (49). Finally, from a technological perspective, currently, IVIM image acquisition methods include free-breathing, breath-hold, and respiratory triggering. Respiratory triggering is used widely in clinical work and can produce high image quality and perfect signal-noise ratio compared with free-breathing and breath-hold; however, a disadvantage of respiratory triggering is that its parametric reproducibility is inferior to the latter two methods. We used respiratory triggering in our study, while Klaus et al. (27) applied breath-hold in their research; thus, respiratory triggering could be a latent contributor to the discrepancy. There is no consensus as to which method is better, because many authors have obtained excellent and interpretative results after using different methods. Thus, more effort is needed to establish standard guidelines.

In conclusion, IVIM provides a new modality to differentiate the HCC and FNH.  $ADC_{total}$  and D demonstrated outstanding and comparable diagnosing performance.

#### Conflict of interest disclosure

The authors declared no conflicts of interest.

#### References

- Marin D, Brancatelli G, Federle MP, et al. Focal nodular hyperplasia: typical and atypical MRI findings with emphasis on the use of contrast media. *Clin Radiol* 2008; 63:577–585. [CrossRef]
- Onur MR, Çiçekçi M, Kayalı A, Poyraz AK, Kocaçoç E. The role of ADC measurement in differential diagnosis of focal hepatic lesions. *Eur J Radiol* 2012; 81:e171–176. [CrossRef]

- Eida S, Sumi M, Sakihama N, Takahashi H, Nakamura T. Apparent diffusion coefficient mapping of salivary gland tumors: prediction of the benignancy and malignancy. *AJNR Am J Neuroradiol* 2007; 28:116–121.
- Le Bihan D, Breton E, Lallemand D, Aubin ML, Vignaud J, Laval-Jeantet M. Separation of diffusion and perfusion in intravoxel incoherent motion MR imaging. *Radiology* 1988; 168:497–505. [CrossRef]
- Xiao-ping Y, Jing H, Fei-ping L, et al. Intravoxel incoherent motion MRI for predicting early response to induction chemotherapy and chemoradiotherapy in patients with nasopharyngeal carcinoma. *J Magn Reson Imaging* 2016; 43:1179–1190. [CrossRef]
- Kim HS, Suh CH, Kim N, Choi CG, Kim SJ. Histogram analysis of intravoxel incoherent motion for differentiating recurrent tumor from treatment effect in patients with glioblastoma: initial clinical experience. *Am J Neuroradiol* 2014; 35:490–497. [CrossRef]
- Parente DB, Paiva FF, Oliveira Neto JA, et al. Intravoxel incoherent motion diffusion weighted MR imaging at 3.0 T: assessment of steatohepatitis and fibrosis compared with liver biopsy in type 2 diabetic patients. *PLoS One* 2015; 10:e125653. [CrossRef]
- Chow AM, Gao DS, Fan SJ, et al. Liver fibrosis: An intravoxel incoherent motion (IVIM) study. *J Magn Reson Imaging* 2012; 36:159–167. [CrossRef]
- Grant KB, Agarwal HK, Shih JH, et al. Comparison of calculated and acquired high b value diffusion-weighted imaging in prostate cancer. *Abdom Imaging* 2015; 40:578–586. [CrossRef]
- Hwang EJ, Lee JM, Yoon JH, et al. Intravoxel incoherent motion diffusion-weighted imaging of pancreatic neuroendocrine tumors: prediction of the histologic grade using pure diffusion coefficient and tumor size. *Invest Radiol* 2014; 49:396–402. [CrossRef]
- Yoon JH, Lee JM, Yu MH, Kiefer B, Han JK, Choi BI. Evaluation of hepatic focal lesions using diffusion-weighted MR imaging: Comparison of apparent diffusion coefficient and intravoxel incoherent motion-derived parameters. *J Magn Reson Imaging* 2014; 39:276–285. [CrossRef]
- Ichikawa S, Motosugi U, Ichikawa T, Sano K, Morisaka H, Araki T. Intravoxel incoherent motion imaging of focal hepatic lesions. *J Magn Reson Imaging* 2013; 37:1371–1376. [CrossRef]
- Chiaradia M, Baranes L, Van Nhieu JT, et al. Intravoxel incoherent motion (IVIM) MR imaging of colorectal liver metastases: Are we only looking at tumor necrosis? *J Magn Reson Imaging* 2014; 39:317–325. [CrossRef]
- Wagner M, Doblaz S, Daire JL, et al. Diffusion-weighted MR imaging for the regional characterization of liver tumors. *Radiology* 2012; 264:464–472. [CrossRef]
- Le Bihan D, Breton E, Lallemand D, Grenier P, Cabanis E, Laval-Jeantet M. MR imaging of intravoxel incoherent motions: application to diffusion and perfusion in neurologic disorders. *Radiology* 1986; 161:401–407. [CrossRef]
- Le Bihan D, Turner R. The capillary network: a link between IVIM and classical perfusion. *Magn Reson Med* 1992; 27:171–178. [CrossRef]

17. Chandarana H, Kang SK, Wong S, et al. Diffusion-weighted intravoxel incoherent motion imaging of renal tumors with histopathologic correlation. *Invest Radiol* 2012; 47:688–696. [\[CrossRef\]](#)
18. Liu J, Wan Y, Wang Z, Qi Y, Qu P, Liu Y. Perfusion and diffusion characteristics of endometrial malignancy based on intravoxel incoherent motion MRI at 3.0T: comparison with normal endometrium. *Acta Radiol* 2015; 57:1140–1148. [\[CrossRef\]](#)
19. Lai V, Li X, Lee VHF, Lam KO, Chan Q, Khong PL. Intravoxel incoherent motion MR imaging: comparison of diffusion and perfusion characteristics between nasopharyngeal carcinoma and post-chemoradiation fibrosis. *Eur Radiol* 2013; 23:2793–2801. [\[CrossRef\]](#)
20. Kakite S, Dyvorne H, Besa C, et al. Hepatocellular carcinoma: Short-term reproducibility of apparent diffusion coefficient and intravoxel incoherent motion parameters at 3.0 T. *J Magn Reson Imaging* 2015; 41:149–156. [\[CrossRef\]](#)
21. Andreou A, Koh DM, Collins DJ, et al. Measurement reproducibility of perfusion fraction and pseudodiffusion coefficient derived by intravoxel incoherent motion diffusion-weighted MR imaging in normal liver and metastases. *Eur Radiol* 2013; 23:428–434. [\[CrossRef\]](#)
22. Choi JS, Kim MJ, Choi JY, Park MS, Lim JS, Kim KW. Diffusion-weighted MR imaging of liver on 3.0-Tesla system: effect of intravenous administration of gadoxetic acid disodium. *Eur Radiol* 2010; 20:1052–1060. [\[CrossRef\]](#)
23. Colagrande S, Mazzoni LN, Mazzoni E, Pradella S. Effects of gadoxetic acid on quantitative diffusion-weighted imaging of the liver. *J Magn Reson Imaging* 2013; 38:365–370. [\[CrossRef\]](#)
24. Doblaz S, Wagner M, Leitao HS, et al. Determination of malignancy and characterization of hepatic tumor type with diffusion-weighted magnetic resonance imaging: comparison of apparent diffusion coefficient and intravoxel incoherent motion-derived measurements. *Invest Radiol* 2013; 48:722–728. [\[CrossRef\]](#)
25. Zhu L, Cheng Q, Luo W, Bao L, Guo G. A comparative study of apparent diffusion coefficient and intravoxel incoherent motion-derived parameters for the characterization of common solid hepatic tumors. *Acta Radiol* 2015; 56:1411–1418. [\[CrossRef\]](#)
26. Watanabe H, Kanematsu M, Goshima S, et al. Characterizing focal hepatic lesions by free-breathing intravoxel incoherent motion MRI at 3.0 T. *Acta Radiol* 2014; 55:1166–1173. [\[CrossRef\]](#)
27. Klauss M, Mayer P, Maier-Hein K, et al. IVIM-diffusion-MRI for the differentiation of solid benign and malign hypervascular liver lesions-Evaluation with two different MR scanners. *Eur J Radiol* 2016; 85:1289–1294. [\[CrossRef\]](#)
28. Barbieri S, Donati OF, Froehlich JM, Thoeny HC. Comparison of intravoxel incoherent motion parameters across MR imagers and field strengths: evaluation in upper abdominal organs. *Radiology* 2015; 279:784–794. [\[CrossRef\]](#)
29. Luciani A, Vignaud A, Cavet M, et al. Liver cirrhosis: intravoxel incoherent motion MR imaging—pilot study. *Radiology* 2008; 249:891–899. [\[CrossRef\]](#)
30. Hashimoto K, Murakami T, Dono K, et al. Assessment of the severity of liver disease and fibrotic change: the usefulness of hepatic CT perfusion imaging. *Oncol Rep* 2006; 16:677–683. [\[CrossRef\]](#)
31. Zhang S, Jia Q, Zhang Z, et al. Intravoxel incoherent motion MRI: emerging applications for nasopharyngeal carcinoma at the primary site. *Eur Radiol* 2014; 24:1998–2004. [\[CrossRef\]](#)
32. Deng Y, Li X, Lei Y, Liang C, Liu Z. Use of diffusion-weighted magnetic resonance imaging to distinguish between lung cancer and focal inflammatory lesions: a comparison of intravoxel incoherent motion derived parameters and apparent diffusion coefficient. *Acta Radiol* 2015; 57:1310–1317. [\[CrossRef\]](#)
33. Lewin M, Fartoux L, Vignaud A, Arrivé L, Menu Y, Rosmorduc O. The diffusion-weighted imaging perfusion fraction *f* is a potential marker of sorafenib treatment in advanced hepatocellular carcinoma: a pilot study. *Eur Radiol* 2011; 21:281–290. [\[CrossRef\]](#)
34. Hectors SJ, Wagner M, Besa C, et al. Intravoxel incoherent motion diffusion-weighted imaging of hepatocellular carcinoma: Is there a correlation with flow and perfusion metrics obtained with dynamic contrast-enhanced MRI? *J Magn Reson Imaging* 2016; 44:856–864. [\[CrossRef\]](#)
35. Yoshino N, Yamada I, Ohbayashi N, et al. Salivary glands and lesions: evaluation of apparent diffusion coefficients with split-echo diffusion-weighted MR imaging—initial results. *Radiology* 2001; 221:837–842. [\[CrossRef\]](#)
36. Shinmoto H, Tamura C, Soga S, et al. An intravoxel incoherent motion diffusion-weighted imaging study of prostate cancer. *AJR Am J Roentgenol* 2012; 199:W496–W500. [\[CrossRef\]](#)
37. Cohen AD, Schieke MC, Hohenwarter MD, Schmainda KM. The effect of low b-values on the intravoxel incoherent motion derived pseudodiffusion parameter in liver. *Magn Reson Med* 2015; 73:306–311. [\[CrossRef\]](#)
38. Guiu B, Petit JM, Capitan V, et al. Intravoxel incoherent motion diffusion-weighted imaging in nonalcoholic fatty liver disease: a 3.0-T MR study. *Radiology* 2012; 265:96–103. [\[CrossRef\]](#)
39. Klauss M, Lemke A, Grunberg K, et al. Intravoxel incoherent motion MRI for the differentiation between mass forming chronic pancreatitis and pancreatic carcinoma. *Invest Radiol* 2011; 46:57–63. [\[CrossRef\]](#)
40. Yuan M, Zhang YD, Zhu C, et al. Comparison of intravoxel incoherent motion diffusion-weighted MR imaging with dynamic contrast-enhanced MRI for differentiating lung cancer from benign solitary pulmonary lesions. *J Magn Reson Imaging* 2016; 43:669–679. [\[CrossRef\]](#)
41. Dyvorne H, Jajamovich G, Kakite S, Kuehn B, Taouli B. Intravoxel incoherent motion diffusion imaging of the liver: Optimal b-value subsampling and impact on parameter precision and reproducibility. *Eur J Radiol* 2014; 83:2109–2113. [\[CrossRef\]](#)
42. Patel J, Sigmund EE, Rusinek H, Oei M, Babb JS, Taouli B. Diagnosis of cirrhosis with intravoxel incoherent motion diffusion MRI and dynamic contrast-enhanced MRI alone and in combination: Preliminary experience. *J Magn Reson Imaging* 2010; 31:589–600. [\[CrossRef\]](#)
43. Wu H, Hu M, Liu Z, et al. Intravoxel incoherent motion diffusion-weighted MRI for characterizing regional variability and monitoring serial changes of parameters in rabbit VX2 liver tumors. *J Magn Reson Imaging* 2016; 43:173–180. [\[CrossRef\]](#)
44. Shiota N, Saito K, Sugimoto K, Takara K, Moriyasu F, Tokuyue K. Intravoxel incoherent motion MRI as a biomarker of sorafenib treatment for advanced hepatocellular carcinoma: a pilot study. *Cancer Imaging* 2016; 16:1–6. [\[CrossRef\]](#)
45. Woo S, Lee JM, Yoon JH, Joo I, Han JK, Choi BI. Intravoxel incoherent motion diffusion-weighted MR imaging of hepatocellular carcinoma: correlation with enhancement degree and histologic grade. *Radiology* 2014; 270:758–767. [\[CrossRef\]](#)
46. Hollingsworth KG, Lomas DJ. Influence of perfusion on hepatic MR diffusion measurement. *NMR Biomed* 2006; 19:231–235. [\[CrossRef\]](#)
47. Schmid-Tannwald C, Jiang Y, Dahi F, Rist C, Sethi I, Oto A. Diffusion-weighted MR imaging of focal liver lesions in the left and right lobes. *Acad Radiol* 2013; 20:440–445. [\[CrossRef\]](#)
48. Kwee TC, Takahara T, Niwa T, et al. Influence of cardiac motion on diffusion-weighted magnetic resonance imaging of the liver. *Magn Reson Mater Phy* 2009; 22:319–325. [\[CrossRef\]](#)
49. Lee Y, Lee SS, Kim N, et al. Intravoxel incoherent motion diffusion-weighted MR imaging of the liver: effect of triggering methods on regional variability and measurement repeatability of quantitative parameters. *Radiology* 2015; 274:405–415. [\[CrossRef\]](#)
50. Dijkstra H, Baron P, Kappert P, Oudkerk M, Sijens PE. Effects of microperfusion in hepatic diffusion weighted imaging. *Eur Radiol* 2012; 22:891–899. [\[CrossRef\]](#)